



Alternative High-plasma Beta Regimes of Electron Heat-flux Instabilities in the Solar Wind

R. A. López¹ , M. Lazar^{2,3} , S. M. Shaaban^{2,4} , S. Poedts^{2,5} , and P. S. Moya^{2,6}

¹Departamento de Física, Universidad de Santiago de Chile, Casilla 307, Santiago, Chile; rlopez186@gmail.com

²Centre for mathematical Plasma Astrophysics, KU Leuven, Celestijnenlaan 200B, B-3001 Leuven, Belgium

³Institut für Theoretische Physik, Lehrstuhl IV: Weltraum- und Astrophysik, Ruhr-Universität Bochum, D-44780 Bochum, Germany

⁴Theoretical Physics Research Group, Physics Department, Faculty of Science, Mansoura University, 35516, Mansoura, Egypt

⁵Institute of Physics, University of Maria Curie-Skłodowska, PL-20-031 Lublin, Poland

⁶Departamento de Física, Facultad de Ciencias, Universidad de Chile, Santiago, Chile

Received 2020 June 2; revised 2020 July 30; accepted 2020 August 13; published 2020 September 4

Abstract

Heat transport in the solar wind is dominated by suprathermal electron populations, i.e., a tenuous halo and a field-aligned beam/strahl, with high energies and antisunward drifts along the magnetic field. Their evolution may offer plausible explanations for the rapid decrease of the heat flux with the solar wind expansion, and self-generated instabilities, or so-called “heat flux instabilities” (HFIs), are typically invoked to explain this evolution. This Letter provides a unified description of the full spectrum of HFIs, as prescribed by the linear kinetic theory for high beta conditions ($\beta_e \gg 0.1$) and different relative drifts (U) of the suprathermals. HFIs of different natures are examined, i.e., electromagnetic, electrostatic or hybrid, propagating parallel or obliquely to the magnetic field, etc., as well as their regimes of interplay (co-existence) or dominance. These alternative regimes of HFIs complement each other and may be characteristic of different relative drifts of suprathermal electrons and various conditions in the solar wind, e.g., in the slow or fast winds, streaming interaction regions, and interplanetary shocks. Moreover, these results strongly suggest that heat flux regulation may not involve just one but several HFIs, concomitantly or successively in time. Conditions for a single, well-defined instability with major effects on the suprathermal electrons and, implicitly, the heat flux, seem to be very limited. Whistler HFIs are more likely to occur but only for minor drifts (as also reported by recent observations), which may explain a modest implication in their regulation, shown already in quasilinear studies and numerical simulations.

Unified Astronomy Thesaurus concepts: [Solar wind \(1534\)](#); [Plasma astrophysics \(1261\)](#); [Space plasmas \(1544\)](#)

1. An Introductory Motivation

The solar wind heat flux is mainly attributed to the energetic suprathermal electrons, a diffuse halo present at all pitch angles, and an electron beam, or strahl, directed along the interplanetary magnetic field away from the Sun. Suprathermals may not exceed 10% of the total density, but have high energies (much higher than thermal or core electrons) and significant antisunward drifts (Pilipp et al. 1987; Wilson et al. 2019). The strahl is in general responsible for a major velocity shift between the core and suprathermal electrons (Rosenbauer et al. 1977; Pilipp et al. 1987; Wilson et al. 2019), but recent studies also reveal a relative drift of the halo (Wilson et al. 2019) to be taken into account in certain circumstances; for instance, in the low-speed winds the strahl can be almost absent (Gurgiolo & Goldstein 2017) and the heat is transported by the halo electrons (Pilipp et al. 1987; Pagel et al. 2005; Bale et al. 2013). However, if the strahl is observed then most of the solar wind heat flux is carried by the strahl electrons (Pilipp et al. 1987; Pagel et al. 2005; Graham et al. 2017; Lazar et al. 2020).

The modifications of suprathermal electrons with the solar wind expansion can be directly linked to the variations of heat flux, and are expected to explain the observed dropouts and an accelerated decrease of the heat flux that is more rapid than predicted by an adiabatic decrease of the main plasma parameters. Indeed, the observations reveal an important erosion of the strahl, which declines in relative density and drift, and broadens their pitch-angle distribution with increasing heliocentric distance (Maksimovic et al. 2005; Pagel et al. 2007; Anderson et al. 2012; Graham et al. 2017; Berčić et al. 2019).

The effect of binary collisions on suprathermals is insignificant, but these evolutions may be explained by so-called “heat flux instabilities” (HFIs) that are self-generated by the relative drifts and beaming velocity of suprathermal electrons (Gary & Feldman 1977; Gary et al. 1999a; Pavan et al. 2013; Shaaban et al. 2018a, 2018b; Shaaban et al. 2019a; Vasko et al. 2019; Verscharen et al. 2019a). The resulting wave fluctuations can induce a diffusion of suprathermals in velocity space, contributing to their relaxation, as already shown in numerical simulations (Dum & Nishikawa 1994; Gary & Saito 2007; Kuzichev et al. 2019; López et al. 2019a).

In this Letter we provide a comparative analysis of the full spectrum of HFIs prescribed by the linear kinetic theory for high plasma beta conditions ($\beta \gg 0.1$) and different relative drifts (U) of the suprathermal populations. Such a unified analysis offers new and multiple perspectives for the implication of HFIs in the evolution of suprathermals and, implicitly, of the solar wind heat flux. The current way of thinking, that a single instability can be identified as the principal mechanism of regulation of the heat flux in the solar wind, may require major revisions to include the interplay and/or succession of two or more instabilities.

In Section 2 we introduce the kinetic formalism often adopted in studies of plasma wave dispersion and stability; in our case, this is a typical plasma with two asymmetric counter-drifting populations of electrons. A short description is also provided for the numerical solver allowing us to determine the full spectrum of the unstable solutions, covering all ranges of frequencies, wavenumbers, and angles of propagation. Models

assumed for the zeroth-order velocity distribution are drifting Maxwellian, which enable a standard and simple parameterization of the solar wind electron–proton plasma populations. We are aware of the existence of other more realistic representations, such as Kappa models (Shaaban et al. 2018a) for the halo, or more asymmetric combinations of drifting Maxwellians for a more skewed strahl (Horaites et al. 2018); these would only complicate our analysis but ultimately lead to similar results and conclusions. Adopting drifting Maxwellian keeps the analysis simple and enables straightforward interpretations of the nature, interplay, and dominance of the HFIs. Moreover, such a dual model can reproduce the slow wind core-halo distribution, in the absence of strahl, but may also be relevant for the fast wind core-strahl configuration if the less drifting halo is assimilated to the core population.⁷ The results are presented and discussed in detail in Section 3, considering each alternative unstable regime in part. These regimes have a wide relevance, covering lower drifts and higher thermal spreads reproducing better the halo electrons, or higher drifts and lower thermal spreads specific to the strahl population, and, nevertheless, a series of intermediary states that may be associated with the relaxation of strahl and the formation or/and enhancement of halo (Hammond et al. 1996; Anderson et al. 2012; Graham et al. 2017). The last section summarizes our results and formulates a series of conclusions, which should facilitate our understanding of the observations and make realistic interpretations of HFIs and their implications.

2. Dispersion and Stability

We consider a collisionless quasi-neutral plasma of protons and two electron populations, namely, a dense central or core component (subscript “c”) and a tenuous suprathermal population (subscript “s”) counter-drifting along the ambient magnetic field, assumed to be constant over at least a few maximum wavelengths of the instabilities considered here (e.g., Shaaban & Lazar 2020, and references therein)

$$f_e(v_{\perp}, v_{\parallel}) = \frac{n_c}{n_e} f_c(v_{\perp}, v_{\parallel}) + \frac{n_s}{n_e} f_s(v_{\perp}, v_{\parallel}), \quad (1)$$

where $n_e \approx n_p$ is the total electron number density, and n_c and n_s are the number densities of the core and strahl populations, respectively, satisfying $n_c + n_s = n_e$. This suprathermal population will be called generically “strahl,” but the same analysis may also apply to a core-halo configuration, as explained already above. For both the core ($j=c$) and strahl ($j=s$) populations we adopt a simple standard description (widely used in similar studies) as drifting bi-Maxwellians (Saito & Gary 2007b; Verscharen et al. 2019b)

$$f_j(v_{\perp}, v_{\parallel}) = \frac{\pi^{-3/2}}{\alpha_{\perp j}^2 \alpha_{\parallel j}} \exp \left\{ -\frac{v_{\perp}^2}{\alpha_{\perp j}^2} - \frac{(v_{\parallel} - U_j)^2}{\alpha_{\parallel j}^2} \right\}, \quad (2)$$

where $\alpha_{\perp, \parallel j} = (2k_B T_{\perp, \parallel j} / m_e)^{1/2}$ are components of thermal velocities perpendicular (\perp) and parallel (\parallel) to the background magnetic field, and U_j are drift velocities, which preserve a zero net current $n_s U_s + n_c U_c = 0$. For simplicity, protons are assumed isotropic ($T_{p\perp} = T_{p\parallel}$), nondrifting ($U_p = 0$), and Maxwellian distributed.

⁷ High beta ($\beta_e > 0.5$) instabilities may not be significantly altered by the inclusion of separate halo in this case (Horaites et al. 2018).

Table 1
Plasma Parameters Used in the Present Study

	Strahl (<i>s</i>)	Core Electrons (<i>c</i>)	Protons (<i>i</i>)
n_j/n_i	0.05	0.95	1.0
$T_{j,\parallel}/T_{i,\parallel}$	4.0	1.0	1.0
m_j/m_i	1/1836	1/1836	1.0
$T_{j,\perp}/T_{j,\parallel}$	1.0	1.0	1.0

Note. Other parameters are: $\omega_{pe}/\Omega_e = 100$, $\beta_c = 8\pi n_e T_c / B_0^2 = 2$.

We preset a general dispersion and stability analysis covering the full wavevector spectrum of (unstable) plasma modes propagating at arbitrary angles θ with respect to the background magnetic field ($\mathbf{B}_0 = B_0 \hat{z}$). Without loss of generality the wavevector $\mathbf{k} = k_{\perp} \hat{x} + k_{\parallel} \hat{z}$ is chosen in the x – z plane ($k_{\parallel} = k \cos \theta$ and $k_{\perp} = k \sin \theta$). Our analysis is based on the kinetic Vlasov–Maxwell dispersion formalism, as provided by Stix (1992), and the unstable solutions are found numerically, providing accurate description for the full spectrum of instabilities (e.g., electrostatic (ES), electromagnetic (EM), or hybrid), and various regimes of their co-existence and dominance. We use a complex root finder based on the Müller’s method to locate the solutions of the plasma dispersion tensor. Solutions provided by this code have been validated in previous studies for various kinetic instabilities (Lazar et al. 2019; López et al. 2019b; Shaaban et al. 2019b), and using particle-in-cell simulations in the low- and high-frequency regimes, and also for multi-component plasmas (López et al. 2017; López & Yoon 2017; López et al. 2020; Mícerica et al. 2020).

The present study focuses on the solar wind high plasma beta conditions, i.e., for $\beta_c \gg 0.1$ (more exactly, $\beta_c \gtrsim 1$), that are susceptible to various instabilities combining kinetic and reactive free-energy effects of plasma particles. Plasma parameters used in our analysis are tabulated in Table 1, unless otherwise specified. Note that all these values are relevant for the solar wind high-beta conditions, approaching average values reported by the observations, e.g., for the relative number densities of the electron populations, e.g., $n_s/n_e = 1 - n_c/n_e = 0.05$, temperature contrast $T_s/T_c = 4$, plasma beta $\beta_c = 2$, frequency ratio $\omega_{pe}/|\Omega_e| = 100$, and a realistic proton-electron mass ratio $m_p/m_e = 1836$.

We characterize the HFIs as primarily defined by the main plasma eigenmodes destabilized by the relative drift of suprathermal electron population, e.g., (1) fast-magnetosonic/whistler (FM/W) waves, RH-circular polarized when propagating in parallel direction, (2) Alfvénic modes, LH-circular polarized in parallel direction, and (3) ES beaming instabilities. High-beta electrons ($\beta_{\text{eff}} = 8\pi n_e k_B T_{\text{eff}} / B_0^2 = 8\pi k_B (n_c T_c + n_s T_s) / B_0^2 = \beta_c + \beta_s > 0.1$) present in the solar wind are expected to excite moderate- and high-frequency modes of these branches. The unstable FM/W modes with high frequencies in the range $\Omega_p < \omega_r < |\Omega_e|$ will simply be named whistler heat-flux instabilities (WHFIs), but making the distinction between the (quasi-)parallel and oblique branches of WHFIs (Sentman et al. 1983; Tokar et al. 1984; Gary et al. 1994; Wilson et al. 2009). The instability mechanisms imply resonant or nonresonant interactions with plasma particles, especially electrons, and may determine linear interplay and conversions between different branches of plasma modes. Even in the absence of instabilities, the wave dispersion of EM modes decouples from ES oscillations only for parallel propagation

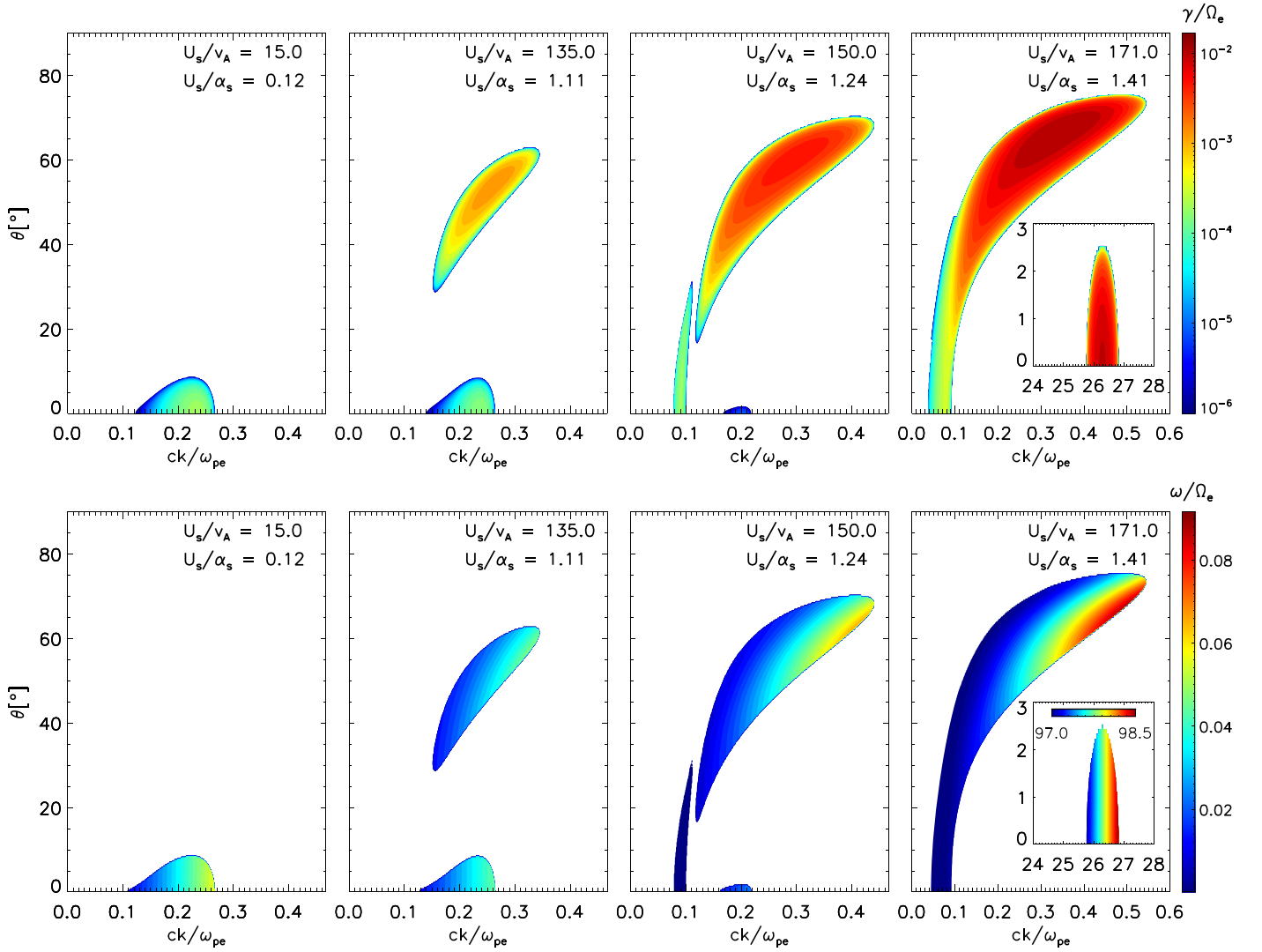


Figure 1. Growth rates γ/Ω_e (top row), and wave frequency ω/Ω_e (bottom row), for $\beta_c = 2.0$ and various drift velocities, $U_s/v_A = 15, 135, 150,$ and 180 .

($\theta = 0$). These aspects will be discussed in the next section, in an attempt to accurately identify the regimes of HFIs and characterize the transition between these regimes.

3. Results

We perform a spectral analysis of the unstable modes in $(ck/\omega_{pe}, \theta)$ -space, where ck/ω_{pe} is the wavenumber normalized to the electron inertial length, and θ is the propagation angle. The top panels in Figure 1 display the full range of the growth rates $\gamma/|\Omega_e| > 0$ (color coded) derived for different drift velocities of the strahl electrons $U_s/v_A = 15$ (left panel), $U_s/v_A = 135$ (middle-left panel), $U_s/v_A = 150$ (middle-right panel), $U_s/v_A = 171$ (right panel). For a nominal value $v_A = 20 \text{ km s}^{-1}$ for the Alfvén speed (usually between 10 and 50 km s^{-1} at 1 au) the highest drifts assumed in Figure 1 correspond to the limit values measured for the relative drift of the electron beam/strahl; see Wilson et al. (2019). The corresponding wave frequency $\omega/|\Omega_e| > 0$ (color coded) is shown in the bottom panels of Figure 1. The Alfvén speed depends only on the ion density and magnetic field, and provides therefore a more neutral normalization, which is common in the literature. However, here we will also explicitly compare the drift of electron strahl U_s with α_s , the thermal

speed of strahl electrons; this is particularly important in the study of kinetic instabilities, directly conditioning their thresholds and dominance regimes, e.g., for the WHFI (Gary 1985; Shaaban et al. 2018a) and the ES instabilities (Gary 1993).

3.1. WHFIs

The left panels in Figure 1 describe the (quasi-)parallel WHFI (Gary 1985; Shaaban et al. 2018a, 2018b; Tong et al. 2019b), which is solely predicted for the parameters chosen in this case, i.e., less energetic strahls with a low drift $U_s = 15v_A = 0.12\alpha_s < \alpha_s$, which is lower than thermal speed of the suprathermal drifting electrons. Although the WHFI also extends to small oblique angles, the fastest growing mode propagates in a direction parallel to the background magnetic field, i.e., $\theta = 0^\circ$. These modes are RH circularly polarized, as shown by the positive polarization (green) in Figure 2. Here the polarization is defined as $\text{Pol} = \text{Re}\{i(E_x/E_y)\text{Sign}(\omega_r)\}$; see Gary (1993).

With increasing drift velocity the growth rate of the parallel WHFI decreases, and this mode becomes eventually damped; see Figure 1, middle-left, middle-right, and right panels for, respectively, $U_s/\alpha_s = 1.11, 1.24,$ and 1.41 . The middle-left panel in Figure 1 presents the unstable solutions for a higher

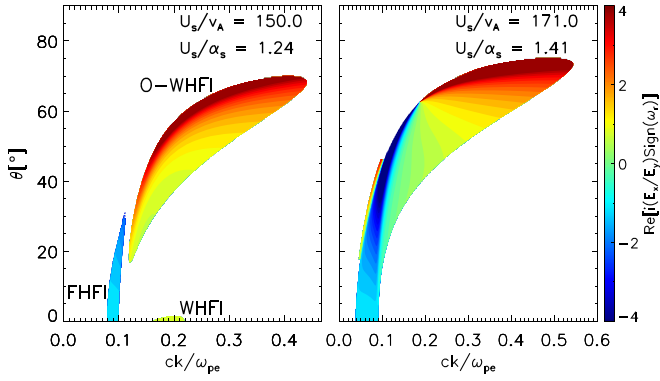


Figure 2. Polarization, $\text{Re}\{i(E_x/E_y)\text{Sign}(\omega_r)\}$, for the last two cases in Figure 1, $U_s/\alpha_s = 1.24$ (left panel) and $U_s/\alpha_s = 1.41$ (right panel).

beaming speed, $U_s = 135v_A = 1.11\alpha_s$, exceeding the thermal speed. The WHFI restrains, but for oblique angles of propagation we find another whistler-like instability, known as the oblique WHFI (O-WHFI; Sentman et al. 1983; Tokar et al. 1984; Wong & Smith 1994; Verscharen et al. 2019b). This oblique mode has a wave frequency dispersion (bottom row) quite similar to that of parallel whistlers, specific wave frequencies ($\Omega_p < \omega < |\Omega_e|$) and wavenumbers, and a RH elliptic (positive) polarization for all directions. Polarization is computed (only for the unstable modes, $\gamma > 0$) as $\text{Re}\{i(E_x/E_y)\text{Sign}(\omega_r)\}$ and is mapped in Figure 2 and the bottom row of Figure 3. By contrast, the O-WHFI is purely oblique and may reach much higher growth rates. In this case maximum growth rates of the O-WHFI ($\gamma_{\text{max}}/\Omega_e = 1.8 \times 10^{-3}$) are obtained for $\theta = 54^\circ.1$ and $ck/\omega_{pe} = 0.26$. The growth rates of this instability are markedly enhanced by only slightly increasing the drift; see the next two cases in Figure 1. The peaking maximum of the growth rates moves toward higher wavenumbers and larger angles of propagation as the drift velocity increases, i.e., $\gamma_{\text{max}}/\Omega_e = 6.9 \times 10^{-3}$ at $\theta = 60^\circ.7$ and $ck/\omega_{pe} = 0.3$ for $U_s/\alpha_s = 1.24$, and $\gamma_{\text{max}}/\Omega_e = 1.7 \times 10^{-2}$ at $\theta = 66^\circ.4$ and $ck/\omega_{pe} = 0.34$ for $U_s/\alpha_s = 1.41$.

Figure 3 provides more detail on the gradual transition from the regime of WHFI, predicted in quasi-parallel directions, to the regime dominated by the O-WHFI. The limb of O-WHFI extending to highly oblique angles forms and detaches from the standard WHFI, which remains at lower angles. These oblique whistlers can be destabilized by the asymmetric counter-drifting populations of electrons specific to the upstream conditions of the interplanetary shocks (Sentman et al. 1983; Tokar et al. 1984; Wong & Smith 1994) and to the fast winds (Verscharen et al. 2019b). In simulations of a predefined low-scale whistler turbulence the oblique whistlers were found able to strongly interact with strahl electrons, contributing to their pitch angle and energy scattering (Saito et al. 2008). Typical fluctuations of oblique whistlers were also reported by the observations in the magnetosphere during magnetically active periods (Wilson et al. 2011), in association with electron beams in interplanetary high- β shocks (Breneman et al. 2010; Ramírez Vélez et al. 2012; Wilson et al. 2012) and recently, collocated with magnetic field holes in the outer corona (Agapitov et al. 2020).

Figure 4 displays the wavenumber dispersion of the electric and magnetic powers for the fastest growing O-WHFI ($\theta = 60^\circ.7$) in Figure 1, the third case ($U_s/\alpha_s = 1.24$). We show the field components in the cartesian (x, y, z) representation (bottom row), and with respect to the wavevector \mathbf{k} , the longitudinal (subscript

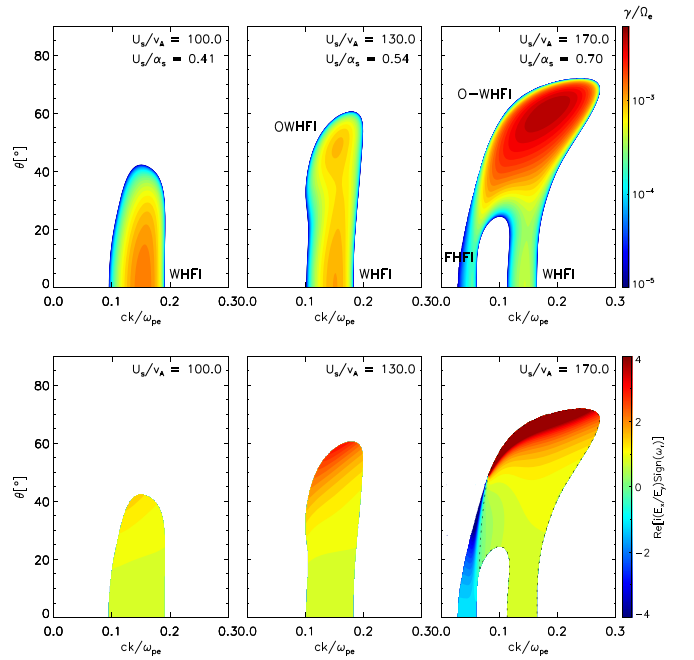


Figure 3. Transition from the WHFI regime to the dominance of O-WHFI. Growth rate (top row) and polarization $\text{Re}\{i(E_x/E_y)\text{Sign}(\omega_r)\}$ (bottom row) as a function of wavenumber for $\beta_c = 8$ and various drift velocities. The dotted black line indicates the contour of minimum polarization (≈ 0.0).

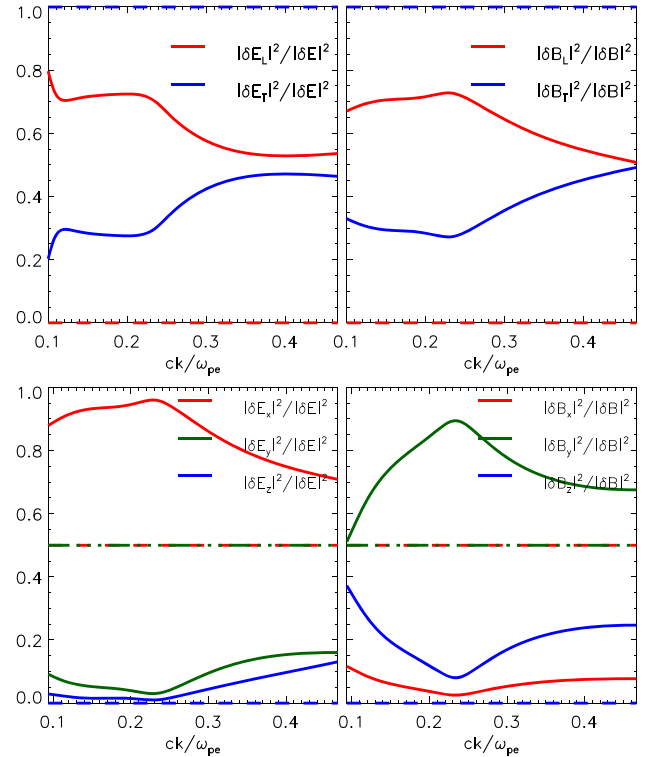


Figure 4. Electric and magnetic field powers for the fastest growing O-WHFI, $\theta = 60^\circ.7$, as seen in Figure 1, the third case for $U_s/\alpha_s = 1.24$ ($U_s/v_A = 150$). Here the directions longitudinal (L) and transverse (T) are defined with respect to the wavevector, $\delta E_L = (\delta \mathbf{E} \cdot \mathbf{k})\mathbf{k}$. Dashed lines show the magnetic/electric powers of WHFI at $\theta = 0^\circ$.

L) or transverse (subscript T) components (top row). Dashed lines correspond to the WHFI at $\theta = 0^\circ$, as expected for the purely transverse (electric and magnetic) fields propagating in parallel direction. Based on this understanding, we can claim that

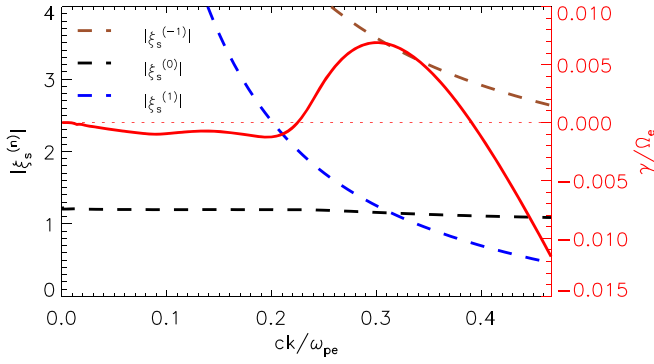


Figure 5. Arguments of plasma dispersion functions $|\xi_s^{(m)}|$ (absolute value) quantifying Landau and transit time resonances $|\xi_s^{(0)}| \rightarrow 1$, and cyclotron resonances $|\xi_s^{(\pm 1)}| \rightarrow 1$, for the fastest growing O-WHFI in Figure 1, top middle-right panel. The growth rate is overplotted with a solid red line.

O-WHFI can be driven cumulatively by the resonant interactions with beaming electrons, via their Landau and transit time resonances with longitudinal (ES) component E_L , and an anomalous cyclotron resonance with transverse (EM) component E_T . The wave-particle resonant mechanisms governing this instability (Tokar et al. 1984) can be identified following the same wavenumber dispersion of the arguments of plasma dispersion function (absolute values) $|\xi_s^{(m)}|$, known as “resonant factors” (Gary et al. 1975). These arguments are computed in Figure 5 for the fastest growing O-WHFI, the same as in the third case in Figure 1 ($U_s = 1.24\alpha_s$). The growth rate is overplotted with a solid red line. For wavenumbers corresponding to the maximum growth rate both resonance conditions are well satisfied, i.e., $|\xi_s^{(0)}| \rightarrow 1$ involving the Landau and/or transit time resonances, and $|\xi_s^{(\pm 1)}| \rightarrow 1$ for the anomalous cyclotron resonance. We already know that the anomalous cyclotron resonance can be responsible for the excitation of WHFI, forward propagating modes being overtaken by the strahl electrons (Tokar et al. 1984; Shaaban et al. 2018a). It is also expected to dominate the mechanism driving O-WHFI at low angles of propagation (mainly involving E_x field component in Figure 4). Instead, highly oblique whistlers are mainly destabilized by the interaction of beaming electrons with the ES and compressive components, through, respectively, a Landau resonance with E_z (which is minor but increases with increasing the wavenumber in Figure 4, bottom row), and a transit time resonance with B_z (which is not minor and shows the similar enhancement with increasing the wavenumber in Figure 4, bottom row). For more explanations see Gary et al. (1975) or the textbook of Gary (1993) and references therein.

3.2. Firehose-like Instabilities of Alfvénic Waves

Another unstable solution obtained for higher drifts, e.g., the last two cases in Figure 1, for $U_s/\alpha_s = 1.24$ and 1.41, is the so-called firehose heat flux instability (FHFI). This mode belongs to the Alfvénic branch, and in a parallel direction it exhibits a maximum growth rate and LH-circular polarization; see also Figures 2 and 3 (Shaaban et al. 2018a, 2018b). The last two cases in Figure 1 show the growth rate (top) and wave frequency (bottom) of the FHFI, located in a narrow interval of low wavenumbers and low frequencies. Growth rates are in general lower than those of the O-WHFI, and maximums peak at $\theta = 0^\circ$. New detailed descriptions of the parallel FHFI, including comparisons with the WHFI and the effects of

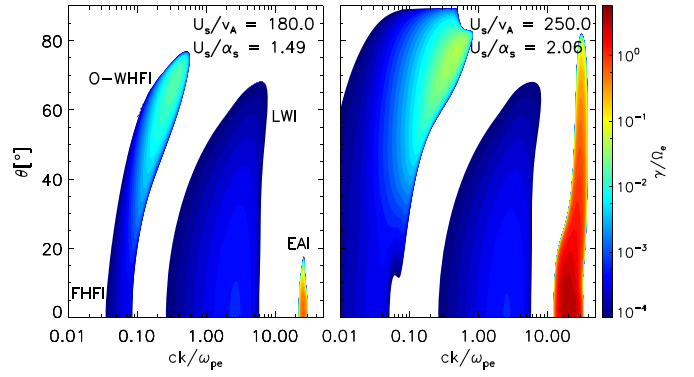


Figure 6. Linear growth rates, γ/Ω_e , ω/Ω_e , for $\beta_c = 2.0$, and drift velocities $U_s/\alpha_s = 1.49$ (left panel) and $U_s/\alpha_s = 2.06$ (right panel).

suprathermal electrons present in the solar wind, can be found in Shaaban et al. (2018a, 2018b). The last case in Figure 1 ($U_s/\alpha_s = 1.41$) shows the growth rates of FHFI extending to more oblique angles and overlapping with the O-WHFI. However, a distinction can easily be made between the LH-polarization of FHFI, i.e., negative values, and the RH-polarization of the O-WHFI, i.e., positive values, in Figures 2 and 3. Moreover, the O-WHFI is by far the more dominant, exhibiting much higher growth rates than FHFI. The middle panels in Figure 1 identify the regime of dominance of the O-WHFI, when this instability exhibits growth rates much higher than other modes, e.g., WHFI or FHFI. However, for higher drifts, e.g., the last case in Figure 1 (for $U_s = 1.41\alpha_s$), the O-WHFI is already competed by the ES instabilities, showing maximum growth rates for parallel propagation.

3.3. ES Instabilities

The ES plasma modes are destabilized when the relative drift of electron strahl is large enough, e.g., $U_s > \alpha_s > \alpha_c$, to ensure Landau resonance with electrons satisfying $\gamma \propto \partial f_s / \partial v_{\parallel} > 0$. Thus, the theory predicts a bump-on-tail instability of Langmuir waves (LWs) for $U_s/\alpha_s < (n_e/n_s)^{1/3}$, or a more reactive electron beam instability (EBI) for $U_s/\alpha_s > (n_e/n_s)^{1/3}$ (Gary 1993). For highly contrasting electron populations with $T_s > T_c$ the electron acoustic (EA) waves become a normal mode, and can be destabilized by a relative core-strahl drift several times higher than thermal speed of the core electrons (Gary 1987, 1993). These instabilities are widely invoked in space plasma applications to explain EA emissions detected in the Earth’s bow shock (Lin et al. 1985), radio bursts associated with bump-on-tail instability of coronal or interplanetary shock-reflected electrons (Nindos et al. 2008), and the broadening of solar wind strahls by self-generated LWs (Pavan et al. 2013) or fast-growing electron beam modes (An et al. 2017; Lee et al. 2019).

The last case in Figure 1 shows the electron acoustic instability (EAI) within built-in panels, with growth rates peaking at $\theta = 0^\circ$ ($\gamma_{\max}/\Omega_e = 1.4 \times 10^{-2}$) and competing with those of the O-WHFI. In this case drift velocity is $U_s/\alpha = 1.41 < (n_e/n_s)^{1/3} \simeq 2.71$ and also satisfies conditions for a Langmuir wave instability (LWI—not shown in Figure 1) with growth rates much lower than EAI; see Figure 6. The left panel in Figure 6 shows the unstable solutions for a slightly higher drift $U_s/\alpha_s = 1.49$, with the EAI in a narrow wavenumber interval but with growth rates much higher than

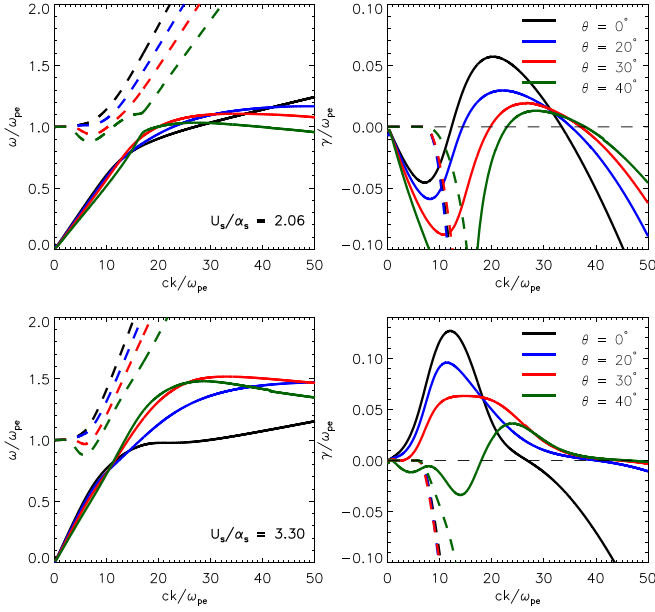


Figure 7. Wave-frequency and growth rate dispersion of the ES instabilities: EAI (solid lines with $\gamma > 0$), and LWI (dashed lines with $\gamma > 0$), for $U_s/\alpha_s = 2.06$ (top row), and 3.30 (bottom row).

both the O-WHFI and LWI. Note also that the FHFI extends to even larger angles, but maximum growth rates remain much less than those of the O-WHFI. The LWI and EAI excite waves with frequencies close to the electron plasma frequency ($\omega \sim \omega_{pe} \simeq \omega_{pc}$), but wavenumbers specific to EAI are one order of magnitude higher; see Figures 6 and 7.

Figure 7 describes the unstable ES modes for $U_s/\alpha_s = 2.06$ (top row, the same as the right panel of Figure 6), and for $U_s/\alpha_s = 3.03$ (bottom row). Specific to more energetic flows and coronal ejections, these high drifts are assumed to be at the origin of coronal and interplanetary bursts. In Figure 7 we show the wave frequency (left) and imaginary frequency (right) for various angles of propagation, this time normalized by the electron plasma frequency. It thus becomes clear that the fastest growing mode is obtained for parallel propagation, and characteristic frequencies are around the electron plasma frequency. These details enable us to clarify the differences shown by the peaking growth rates in Figure 6. By increasing the drift, maximum growth rates remain in a parallel direction, but extend to lower wavenumbers and lower frequencies characteristic to the EBI ($\omega_r \simeq kU_s$). The most unstable modes result from the interplay of EAI and EBI at low angles, and EAI remains solely responsible for the lower growth rates obtained at oblique angles only. In the second case ($U_s/\alpha_s = 3.30$) in Figure 7 we can distinguish two peaks of the imaginary frequency γ , which correspond to the EBI and EAI when $\gamma > 0$.

The opinions regarding the implication of ES beaming-like instabilities in the regulation of electron strahl are in general divided (Gary et al. 1975; Pavan et al. 2013; Verscharen et al. 2019a). In this section we clearly show that energetic strahls may provide favorable conditions for these instabilities to develop, identifying the following representative regimes. The last case in Figure 1 describes a transition between the O-WHFI and the EAI, when both of these types of fluctuations are expected to interplay. For higher drifts, i.e., in the left panel of

Figure 6, the HFIs are dominated by the EAI, while for even higher drifts the right panel in Figure 6 shows another transitory regime, from EAI to EBI. The EBI is expected to dominate the unstable regimes for the highest drifts considered in Figure 7 (bottom row) satisfying $U_s/\alpha_s > (n_e/n_s)^{1/3} \simeq 2.71$.

3.4. Drift and Beta Instability Thresholds

We have already identified and characterized a series of alternative regimes of HFIs, as predicted by the theory for different relative drifts of the electron strahl (satisfying the zero net current condition). The parametric analysis is completed here with a description of the instability thresholds, which highly depend on the electron plasma beta (limiting to high-beta conditions, $\beta > 0.1$). Such a general perspective is provided in Figures 8 and 9 by the contours of maximum growth rates γ_{\max}/Ω_e , which are derived in terms of drift velocities for the strahl (U_s) or core (U_c) and the core plasma beta (β_c). Note that these contours have no information about θ or k , as they represent the maximum growth rates from the full spectrum of unstable modes (including all frequencies, wavenumbers and angles of propagation) obtained for each combination of drift and electron plasma beta.

Figure 8 presents contours of maximum growth rates for the WHFI (left panels), FHFI (middle panels), and O-WHFI (right panels). These are derived in terms of the core electron beta (β_c) and the drift velocity, expressed as U_s/α_s (top), or $-U_c/v_A$ and U_s/v_A (bottom row). There are unstable regimes that appear in both cases, but complementary regimes are also shown; for instance, those hidden by a direct dependence of β_c on v_A (via the density and magnetic field) are shown in the top row, while those hidden by a more subtle dependence of β_c on α_s (due to a fixed core-strahl temperature contrast $T_c/T_s = 1/4$; see Table 1, leading to $\alpha_c = (T_c/T_s)^{1/2}\alpha_s$) appear in the bottom row. On the other hand, the variations of relative drifts with respect to thermal speed α_s (top row) may have an extended physical relevance, helping us not only to delimit complementary regimes corresponding to different instabilities, e.g., WHFI from FHFI, or even from ES instabilities, but also to understand the difference between the physical mechanisms responsible for these instabilities (as discussed above).

The left panels in Figure 8 show a non-monotonous variation of the growth rate of WHFI with the drift velocity, as the growth rate increases and then decreases with increasing the drift. Consequently, the most unstable solutions of WHFI are located in between the lower and upper thresholds, as also found by Shaaban et al. (2018a, 2018b) for lower $\beta_c \lesssim 1$ plasma conditions. Complementary to WHFI, for higher drifts the theory predicts two distinct instabilities. The middle panels of Figure 8 show the maximum growth rates of FHFI, with a monotonous variation with the drift velocity, and the core plasma beta (β_c). The maximum growth rate γ_{\max}/Ω_e of FHFI increases with the drift velocity, but decreases as β_c increases (bottom row). The most unstable FHFI is located at large drifts (U_c) and low β_c . The right panels in Figure 8 show the O-WHFI, mostly overlapping with the parametric regime of FHFI, but the O-WHFI exhibits much higher maximum growth rates than FHFI and WHFI. Similar to FHFI, the maximum growth rate of the O-WHFI is, in general, a monotonous function of the drift velocity and core plasma beta. The O-WHFI is stimulated by increasing the drift velocity and decreasing the core plasma beta. For low beta the most unstable O-WHFI is located at large drifts, but with increasing the

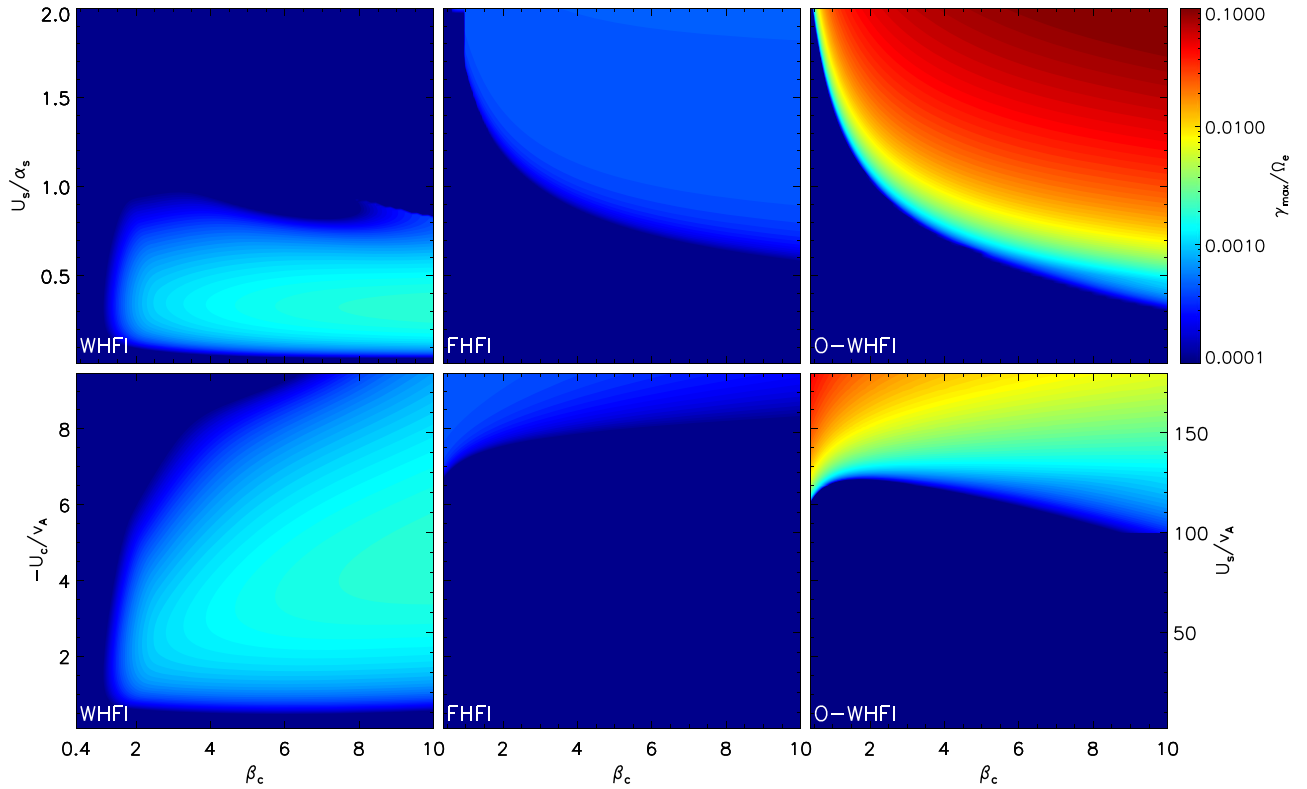


Figure 8. Maximum growth rates (color coded) as a function of β_c and U_s/α_s (top row), or $-U_c/v_A$ and U_s/v_A (bottom row) for the WHFI (left panels), FHF (middle panels), and O-WHFI (right panels).

plasma beta this instability becomes operative for lower drift velocities. The lowest drifts remain susceptible only to WHFI.

The alternative regimes of EM instabilities described in Figure 8 are contrasted in Figure 9 with the very high growth rates of ES instabilities. The range of plasma beta is extended to the interval $0.1 \leq \beta_c \leq 10$, to include lower beta conditions. For moderately high values of beta (e.g., $\beta_c = 2$), WHFI and O-WHFI are complementary; their regimes, at the lowest or higher drifts velocities, respectively, are well delimited by the lowest contour levels of γ_{\max} . For higher values of β_c these two regimes overlap, in between defining a transition where WHFI and O-WHFI interplay and may compete to each other. The lower beta part of the figure is dominated by the ES instabilities, which involve the EAI and for higher drifts the EBI. These instabilities exhibit very high growth rates, which explains the abrupt transition to the O-WHFI. Marked with white dashed lines at about $U_s/\alpha_s \simeq \sqrt{2}$, these narrow threshold conditions are characteristic of the interplay between O-WHFI and EAI described in the last case of Figure 1. For our parameterization characteristic to the solar wind, the growth rate of FHF is always smaller than the O-WHFI or EAI, and we could not find any regime where FHF can develop.

Finally, in Figure 10 we show the effect of the strahl-core temperature ratio, contrasting maximum growth rates obtained for lower and higher values, respectively, $T_s/T_c = 3$ in the top panel and $T_s/T_c = 5$ in the bottom panel. These values are in the range of solar wind measurements (Wilson et al. 2019). Major differences are observed for the WHFI thresholds. For higher ratios T_s/T_c , the region of dominance of the WHFI extends to lower betas and higher drifts (as also shown in Figure 8 for the case $T_s/T_c = 4$) covering a larger portion of

the parameter space. The region of co-existence of WHFI and O-WHFI also extends to lower values of β_c , while the O-WHFI region of dominance remains almost unchanged, although the maximum growth rates of this instability decrease as the temperature ratio increases.

4. Conclusions

We have provided a unified description of the full spectrum of HFIs driven by the relative drift of suprathermal electron populations under the high-beta solar wind conditions. Their nature, wave dispersion, stability, and polarization highly depend on the relative drift (or beaming) velocity of suprathermal electrons and the plasma beta parameter. The zeroth-order drifting counter-drifting distributions are modeled with standard drifting Maxwellians, which enable simple parameterizations and straightforward analysis and interpretation of HFIs in various conditions typically encountered in the solar wind, e.g., a drifting halo in the slow wind, or the electron strahl carrying the heat flux of the high speed flows.

The unstable solutions have been derived and examined in terms of their main features, i.e., wave frequencies, growth rates, wavenumbers, and propagation angles, and in terms of plasma (electron) parameters defining the instability conditions, thresholds, etc. Three EM instabilities are predicted: the quasi-parallel WHFI, the FHF, and the O-WHFI, and a series of ES instabilities destabilizing LWs, the EA modes, or the more reactive EBI.

We can identify three alternative regimes, each of them characterized by a well-defined instability, solely predicted by the theory or with (maximum) growth rates much higher than other unstable modes. Thus, for relatively low drifts of

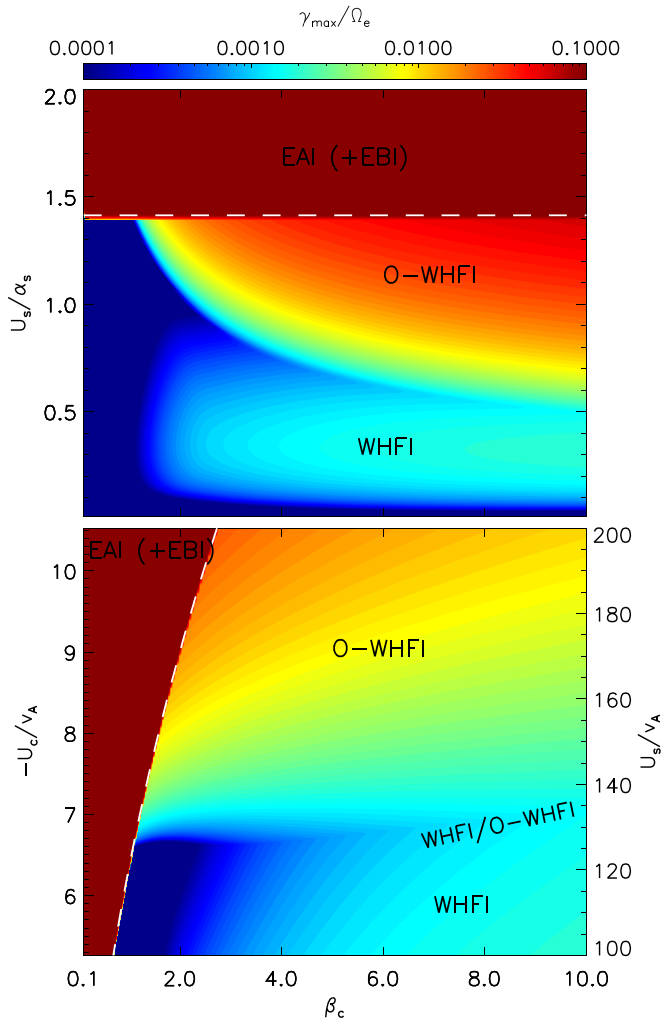


Figure 9. Maximum growth rate as a function of core plasma beta and beam velocity, β_c versus U_s/α_s (top panel), and $-U_c/v_A$ and also U_s/v_A (bottom panel), for all the instabilities discussed, WHFI, FHFI, O-WHFI, and EAI (plus EBI). The dashed white line indicates $U_s/\alpha_s = \sqrt{2}$.

suprathermal electrons, i.e., $U_s < \alpha_s$, the WHFI is the only operative, with maximum growth rates associated with parallel propagation. This regime is characteristic of the low drifts and the large quasithermal spread of halo electrons, and seems to be controlled exclusively by the WHFI (Gary 1985; Scime et al. 1994; Shaaban et al. 2018a). Typical WHF fluctuations associated with drifting suprathermal populations are confirmed by the solar wind observations; see Wilson et al. (2013) and Tong et al. (2019b, 2019a).

For higher drifts the dominance shifts to the O-WHFI, which are hybrid modes triggered unstable by cyclotron resonance, mainly at small angles of propagation, combined with Landau and transit time resonances that are dominant at larger angles (Sentman et al. 1983; Tokar et al. 1984; Wong & Smith 1994; Verscharen et al. 2019b). With increasing the drift the instabilities become more specific to a core-strahl configuration, switching from a kinetic nature near the threshold to a more reactive type for higher drifts. The growth rate of O-WHFI increases with the drift, and is in general higher (or even much higher) than that of the WHFI. The wave fluctuations resembling oblique whistlers are indeed associated with electron beams in the solar wind observations (Breneman et al. 2010; Ramírez Vélaz et al. 2012; Wilson et al. 2012). The

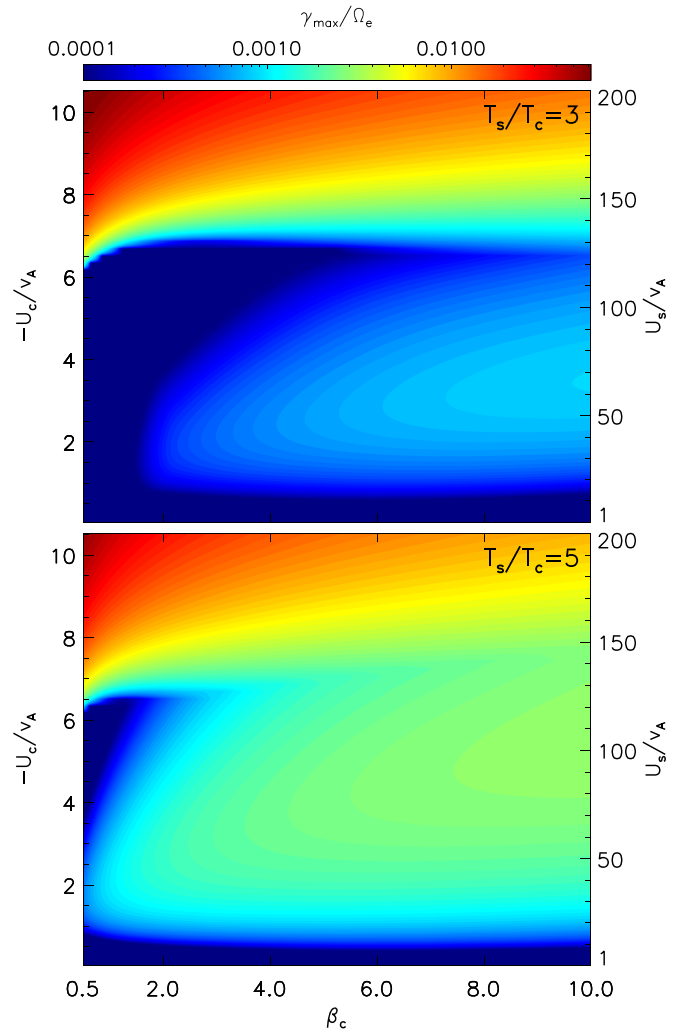


Figure 10. Maximum growth rate as a function of core plasma beta and beam velocity, $-U_c/v_A$ and U_s/v_A , for different temperature ratios between core and strahl, $T_s/T_c = 3$ and 5.

increase of temperature contrast (T_s/T_c) slightly inhibits the growth rates of O-WHFI, but stimulates the WHFI extending the instability conditions to lower plasma betas. The effect is similar to that caused by a decrease of the relative drift, leading to a regime more specific to the halo electrons.

Theoretically, the ES modes can be destabilized already for $U_s > \alpha_s$; for instance, conditions for a bump-on-tail instability can be satisfied for $\alpha_s < U_s < (n_e/n_s)^{1/3}\alpha_s (\simeq 2.71\alpha_s)$ to excite LWs. However, in the given conditions these modes may not have any chance to develop because their growth rates are much lower than those of the O-WHFI predicted for the same conditions. Instead, due to the temperature contrast between electron populations another instability is predicted, namely, the EAI triggered by drifting electrons with $U_s \geq \sqrt{2}\alpha_s$ (when $\beta_e = 2$). Near the threshold this instability strongly competes with the O-WHFI, while for slightly higher drifts the growth rates of EAI is already very large, with peaking values at least one order of magnitude higher than those of the O-WHFI. For even more energetic beams satisfying $U_s > (n_e/n_s)^{1/3}\alpha_s (\simeq 2.71\alpha_s)$, which are relevant for the fast outflows in the outer corona (also coronal mass ejections), the theory predicts an additional EBI. Near the threshold of this instability we found four unstable modes, O-WHFI, LWI, EAI, and EBI, but only the last two have



the opportunity to develop, and have comparable growth rates that are much higher than those of the other two modes. These kind of ES instabilities are widely invoked in space plasma applications, but the resulting high-amplitude fluctuations may undergo rapid nonlinear decays and are ultimately witnessed by the EM or radio emissions; see Nindos et al. (2008) and references therein.

In summary, our results identify three complementary regimes of HFIs associated to three distinct instabilities, the parallel WHFI, the O-WHFI, and the EAI, and interlinked by a series of transitory regimes. For each transition the theory predicts the interplay or co-existence of at least two distinct instabilities; for instance, the interplay of parallel and oblique whistlers for lower drifts, a mixing of the O-WHFI and EAI with an increase in drift, or the limit case, where the EAI and EBI can develop concomitantly. These findings strongly suggest that heat-flux regulation may not involve one but several HFIs, concomitantly or successively in time. Conditions for a single, well-defined instability with major effects on the suprathermal electrons and, implicitly, the heat flux, may be very limited. Whistler HFIs are more likely to occur but only for minor drifts (as also reported by recent observations), which may explain a modest implication in their regulation, shown already in quasilinear studies (Shaaban et al. 2019a, 2019b) and numerical simulations (López et al. 2019a).

We conclude by stating that a realistic plasma parameterization, combined with a selective spectral analysis, is crucial for understanding the nature and origin of HFIs and their implication in the regulation of the solar wind heat flux. Our theoretical predictions are expected to stimulate further investigations using full kinetic simulations and confirm the existence of these alternative regimes, not only in the initial linear phase of HFIs but also during their quasi- or nonlinear growth in time, which involves a relaxation of the relative drift and, implicitly, changes to different successive regimes of HFIs corresponding to lower drifts.

These results were obtained in the framework of the projects SCHL 201/35-1 (DFG-German Research Foundation), C14/19/089 (C1 project Internal Funds KU Leuven), G.OA23.16N (FWO-Vlaanderen), and C 90347 (ESA Prodex). R.A.L acknowledges the support of AFOSR grant FA9550-19-1-0384. S.M. Shaaban acknowledges support by a FWO Postdoctoral Fellowship, grant No. 12Z6218N. P.S. Moya is grateful for the support of KU Leuven BOF Network Fellowship NF/19/001, and ANID Chile through FONDECYT grant No. 1191351.

ORCID iDs

R. A. López  <https://orcid.org/0000-0003-3223-1498>
 M. Lazar  <https://orcid.org/0000-0002-8508-5466>
 S. M. Shaaban  <https://orcid.org/0000-0003-0465-598X>
 S. Poedts  <https://orcid.org/0000-0002-1743-0651>
 P. S. Moya  <https://orcid.org/0000-0002-9161-0888>

References

Agapitov, O. V., de Wit, T. D., Mozer, F. S., et al. 2020, *ApJL*, **891**, L20
 An, X., Bortnik, J., Van Compernelle, B., Decyk, V., & Thorne, R. 2017, *PhPI*, **24**, 072116
 Anderson, B. R., Skoug, R. M., Steinberg, J. T., & McComas, D. J. 2012, *JGRA*, **117**, A04107

Bale, S. D., Pulupa, M., Salem, C., Chen, C. H. K., & Quataert, E. 2013, *ApJL*, **769**, L22
 Berčić, L., Maksimović, M., Land, i. S., & Matteini, L. 2019, *MNRAS*, **486**, 3404
 Breneman, A., Cattell, C., Schreiner, S., et al. 2010, *JGRA*, **115**, A08104
 Dum, C. T., & Nishikawa, K. I. 1994, *PhPI*, **1**, 1821
 Gary, S. P. 1985, *JGR*, **90**, 10815
 Gary, S. P. 1987, *PhFI*, **30**, 2745
 Gary, S. P. 1993, *Theory of Space Plasma Microinstabilities* (New York: Cambridge Univ. Press)
 Gary, S. P., & Feldman, W. C. 1977, *JGR*, **82**, 1087
 Gary, S. P., Feldman, W. C., Forslund, D. W., & Montgomery, M. D. 1975b, *JGR*, **80**, 4197
 Gary, S. P., & Saito, S. 2007, *GeoRL*, **34**, L14111
 Gary, S. P., Scime, E. E., Phillips, J. L., & Feldman, W. C. 1994, *JGR*, **99**, 23391
 Gary, S. P., Skoug, R. M., & Daughton, W. 1999a, *PhPI*, **6**, 2607
 Graham, G. A., Rae, I. J., Owen, C. J., et al. 2017, *JGRA*, **122**, 3858
 Gurgiolo, C., & Goldstein, M. L. 2017, *AnGeo*, **35**, 71
 Hammond, C. M., Feldman, W. C., McComas, D. J., Phillips, J. L., & Forsyth, R. J. 1996, *A&A*, **316**, 350
 Horaites, K., Astfalk, P., Boldyrev, S., & Jenko, F. 2018, *MNRAS*, **480**, 1499
 Kuzichev, I. V., Vasko, I. Y., Soto-Chavez, A. R., et al. 2019, *ApJ*, **882**, 81
 Lazar, M., López, R. A., Shaaban, S. M., Poedts, S., & Fichtner, H. 2019, *Ap&SS*, **364**, 171
 Lazar, M., Scherer, K., Fichtner, H., & Pierrard, V. 2020, *A&A*, **634**, A20
 Lee, S.-Y., Lee, E., & Yoon, P. H. 2019, *ApJ*, **876**, 117
 Lin, C. S., Winske, D., & Tokar, R. L. 1985, *JGR*, **90**, 8269
 López, R. A., Lazar, M., Shaaban, S. M., et al. 2019b, *ApJL*, **873**, L20
 López, R. A., Lazar, M., Shaaban, S. M., Poedts, S., & Moya, P. S. 2020, *PPCF*, **62**, 075006
 López, R. A., Shaaban, S. M., Lazar, M., et al. 2019a, *ApJL*, **882**, L8
 López, R. A., Viñas, A. F., Araneda, J. A., & Yoon, P. H. 2017, *ApJ*, **845**, 60
 López, R. A., & Yoon, P. H. 2017, *PPCF*, **59**, 115003
 Maksimovic, M., Zouganelis, I., Chaufray, J. Y., et al. 2005, *JGRA*, **110**, A09104
 Micera, A., Boella, E., Zhukov, A. N., et al. 2020, *ApJ*, **893**, 130
 Nindos, A., Aurass, H., Klein, K. L., & Trottet, G. 2008, *SoPh*, **253**, 3
 Pagel, C., Crooker, N. U., Larson, D. E., Kahler, S. W., & Owens, M. J. 2005, *JGRA*, **110**, A01103
 Pagel, C., Gary, S. P., de Koning, C. A., Skoug, R. M., & Steinberg, J. T. 2007, *JGRA*, **112**, A04103
 Pavan, J., Viñas, A. F., Yoon, P. H., Ziebell, L. F., & Gaelzer, R. 2013, *ApJL*, **769**, L30
 Pilipp, W. G., Miggenrieder, H., Montgomery, M. D., et al. 1987, *JGR*, **92**, 1075
 Ramírez Vélez, J. C., Blanco-Cano, X., Aguilar-Rodríguez, E., et al. 2012, *JGRA*, **117**, A11103
 Rosenbauer, H., Schwenn, R., Marsch, E., et al. 1977, *JGZG*, **42**, 561
 Saito, S., & Gary, S. P. 2007b, *JGR*, **112**, A06116
 Saito, S., Gary, S. P., Li, H., & Narita, Y. 2008, *PhPI*, **15**, 102305
 Scime, E. E., Bame, S. J., Feldman, W. C., et al. 1994, *JGR*, **99**, 23401
 Sentman, D. D., Thomsen, M. F., Gary, S. P., Feldman, W. C., & Hoppe, M. M. 1983, *JGR*, **88**, 2048
 Shaaban, S. M., & Lazar, M. 2020, *MNRAS*, **492**, 3529
 Shaaban, S. M., Lazar, M., López, R. A., Fichtner, H., & Poedts, S. 2019b, *MNRAS*, **483**, 5642
 Shaaban, S. M., Lazar, M., & Poedts, S. 2018a, *MNRAS*, **480**, 310
 Shaaban, S. M., Lazar, M., Yoon, P., Poedts, S., & López, R. 2019a, *MNRAS*, **486**, 4498
 Shaaban, S. M., Lazar, M., Yoon, P. H., & Poedts, S. 2018b, *PhPI*, **25**, 082105
 Stix, T. H. 1992, *Waves in Plasmas* (New York: AIP)
 Tokar, R. L., Gurnett, D. A., & Feldman, W. C. 1984, *JGR*, **89**, 105
 Tong, Y., Vasko, I. Y., Artemyev, A. V., Bale, S. D., & Mozer, F. S. 2019a, *ApJ*, **878**, 41
 Tong, Y., Vasko, I. Y., Pulupa, M., et al. 2019b, *ApJL*, **870**, L6
 Vasko, I. Y., Krasnoselskikh, V., Tong, Y., et al. 2019, *ApJL*, **871**, L29
 Verscharen, D., Chandran, B. D. G., Jeong, S.-Y., et al. 2019a, *ApJ*, **886**, 136
 Verscharen, D., Klein, K. G., & Maruca, B. A. 2019b, *LRSP*, **16**, 5
 Wilson, L., III, Cattell, C., Kellogg, P., et al. 2009, *JGRA*, **114**, A10106
 Wilson, L. B., III, Cattell, C. A., Kellogg, P. J., et al. 2011, *GeoRL*, **38**, L17107
 Wilson, L. B., III, Koval, A., Szabo, A., et al. 2012, *GeoRL*, **39**, L08109
 Wilson, L. B., III, Koval, A., Szabo, A., et al. 2013, *JGRA*, **118**, 5
 Wilson, L. B. I., III, Chen, L.-J., Wang, S., et al. 2019, *ApJS*, **245**, 24
 Wong, H. K., & Smith, C. W. 1994, *JGR*, **99**, 13373